

Stable and memory-efficient image recovery using monotone operator learning (MOL)

Aniket Pramanik, *Student Member, IEEE*, Mathews Jacob, *Fellow, IEEE*,

Abstract—We introduce a monotone deep equilibrium learning framework for large-scale inverse problems in imaging. The proposed algorithm relies on forward-backward splitting, where each iteration consists of a gradient descent involving the score function and a conjugate gradient algorithm to encourage data consistency. The score function is modeled as a monotone convolutional neural network. The use of a monotone operator offers several benefits, including guaranteed convergence, uniqueness of fixed point, and robustness to input perturbations, similar to the use of convex priors in compressive sensing. In addition, the proposed formulation is significantly more memory-efficient than unrolled methods, which allows us to apply it to 3D problems that current unrolled algorithms cannot handle. Experiments show that the proposed scheme can offer improved performance in 3D settings while being stable in the presence of input perturbations.

Index Terms—Model-based deep learning, Monotone operator learning, Deep equilibrium models.

I. INTRODUCTION

The recovery of images from a few noisy measurements is a common problem in several medical imaging modalities, including MRI [1], CT [2], PET [3], and microscopy [4]. In the undersampled setting, multiple images can give a similar fit to the measured data, making the recovery ill-posed. Compressive sensing (CS) algorithms pose the recovery as a convex optimization problem, where a convex prior is added to the data-consistency term to regularize the recovery [5]. The main benefit of convex priors in CS applications is the uniqueness of the solutions. In particular, the convexity of the priors guarantees that the overall cost function in (3) is convex, even when \mathcal{A} operator has a large null space. Another desirable property of strongly convex priors in CS is the robustness of the solution to input perturbations. In addition, numerous algorithms that rely on the proximal mapping of the priors, which enjoy guaranteed convergence to the solution, also exist.

Aniket Pramanik and Mathews Jacob are from the Department of Electrical and Computer Engineering at the University of Iowa, Iowa City, IA, 52242, USA (e-mail: aniket-pramanik@uiowa.edu; mathews-jacob@uiowa.edu). This work is supported by grants NIH R01 AG067078 and R01 EB031169.

Plug and play (PnP) methods were introduced to significantly improve performance when compared to compressed sensing; PnP methods replace the proximal mapping steps in CS algorithms with off-the-shelf denoisers [6]–[11]. These methods come with convergence guarantees and uniqueness when the data-consistency term is strongly convex [12]. In the CS setting, the data term is not convex; weaker convergence guarantees are available in this case [9], but the uniqueness is not guaranteed. Plug and play methods, which use pre-learned convolutional neural network (CNN) modules instead of off-the-shelf denoisers, have shown to offer improved performance [9], [10]. Another category of approaches relies on unrolled optimization; these algorithms unroll the iterative optimization algorithm used in PnP to obtain a deeper network, which is composed of optimization blocks to promote data consistency and CNN blocks; the resulting deep network is trained in an end-to-end fashion [13]–[15]. By matching the CNN blocks with the specific sampling operator, these methods typically offer better performance than PnP methods [13]–[16]. The unrolling strategy unfortunately results in high memory demand during training; this makes it challenging to apply the algorithm for large-scale optimization schemes. The general practice is to restrict the number of iterations/unrolling steps to keep the memory demand during training and computational complexity during inference low. However, this approach cannot guarantee the convergence of the algorithm.

Deep equilibrium (DEQ) models [17] have been introduced to overcome the above problems with unrolled methods [18]. Current DEQ methods [18] impose non-expansive constraints on the residual CNN blocks to ensure that the forward fixed-point iterations converge to a fixed point. This property allows one to perform forward and backward propagation using fixed-point iteration involving a single physical layer, which significantly reduces the memory demand when compared to unrolling methods. The alternating direction method of multipliers (ADMM) and proximal gradient (PG) DEQ algorithms are associated with convergence guarantees [18] when the data-consistency term is strongly convex. In addition, the convergence analysis requires the residual network

to be non-expansive [18], which is imposed by using spectral normalization of each layer of the network. Our experiments show that spectral normalization often translates to networks with low representation ability, which translates to lower performance. Another challenge with current DEQ methods is the potential non-uniqueness of the fixed point, which can also affect the stability/robustness of the algorithm in the presence of input perturbations. We note that the stability of deep image reconstruction networks is a concern [19]; deep networks are reported to be more fragile to input perturbations than are conventional algorithms.

The main goal of this work is to introduce a DEQ algorithm that shares the desirable properties of convex CS algorithms, including guaranteed uniqueness, robustness, and fast convergence. In addition, the approach inherits the memory efficiency of DEQ algorithms. We introduce a forward-backward algorithm that uses a CNN to learn the score function, which is the derivative of the log prior, unlike current algorithms that replace the proximal mapping of the score function. We constrain the CNN to be a monotone operator and term the resulting algorithm as a monotone operator learning (MOL) scheme. We also introduce guarantees on the robustness of the algorithm to input perturbations. We express the monotone operator \mathcal{F} as a residual block $\mathcal{F} = \mathcal{I} - \mathcal{H}$, where \mathcal{H} is contractive. We use a regularization strategy to restrict the Lipschitz constant of \mathcal{H} . Our experiments show that the regularization strategy can offer algorithms with better performance than schemes that rely on spectral normalization. We implement and validate the framework for a parallel MRI recovery setting. Our experiments show that the proposed algorithm can offer improved performance in large-scale inverse problems. More importantly, unlike current deep learning methods that are fragile to input perturbations, the proposed scheme demonstrates improved stability.

II. BACKGROUND

We consider recovery of an image \mathbf{x} from its noisy undersampled measurements \mathbf{b} , specified by

$$\mathbf{b} = \mathcal{A}(\mathbf{x}) + \mathbf{n}, \quad (1)$$

where \mathcal{A} is a linear operator and $\mathbf{n} \sim \mathcal{N}(\mathbf{0}, \sigma^2 \mathbf{I})$ is an additive white Gaussian noise. The measurement model provides a conditional probability $p(\mathbf{b}|\mathbf{x}) = \mathcal{N}(\mathcal{A}(\mathbf{x}), \sigma^2 \mathbf{I})$. The maximum a posteriori (MAP) estimation of \mathbf{x} from the measurements \mathbf{b} poses the recovery as

$$\mathbf{x}_{\text{MAP}} = \arg \max_{\mathbf{x}} \log p(\mathbf{x}|\mathbf{b}). \quad (2)$$

Using Bayes' rule, $p(\mathbf{x}|\mathbf{b}) \propto p(\mathbf{b}|\mathbf{x})p(\mathbf{x})$ and the monotonicity of the log function, one obtains

$$\mathbf{x}_{\text{MAP}} = \arg \min_{\mathbf{x}} C(\mathbf{x}),$$

where

$$C(\mathbf{x}) = \underbrace{\frac{\lambda}{2} \|\mathcal{A}(\mathbf{x}) - \mathbf{b}\|_2^2}_{\mathcal{D}(\mathbf{x}) = -\log p(\mathbf{b}|\mathbf{x})} + \underbrace{\phi(\mathbf{x})}_{-\log p(\mathbf{x})}. \quad (3)$$

Here, $\lambda = \frac{1}{\sigma^2}$. The first term $\mathcal{D}(\mathbf{x}) = -\log p(\mathbf{b}|\mathbf{x})$ is the data-consistency term, while the second term is the log prior. Compressed sensing algorithms use convex prior distributions (e.g., $\phi(\mathbf{x}) = \|\mathbf{x}\|_{\ell_1}$) to result in a strongly convex cost function with unique minimum.

We note that the minimum of (3) satisfies the fixed-point relation:

$$\underbrace{\lambda \mathcal{A}^H(\mathcal{A}(\mathbf{x}) - \mathbf{b})}_{\mathcal{G}(\mathbf{x})} + \underbrace{\nabla_{\mathbf{x}} \phi(\mathbf{x})}_{\mathcal{F}(\mathbf{x})} = 0, \quad (4)$$

where \mathcal{A}^H is the Hermitian operator of \mathcal{A} . Several algorithms that converge to the fixed point of (4) have been introduced in the CS setting [20]–[22]. For example, forward-backward algorithms rewrite (4) as $(\mathcal{I} + \alpha \mathcal{F})(\mathbf{x}) = (\mathcal{I} - \alpha \mathcal{G})(\mathbf{x})$, $\alpha > 0$, which has the same fixed point as (4). Classical PG algorithms use the iterative rule $\mathbf{x}_{n+1} = (\mathcal{I} + \alpha \mathcal{F})^{-1}(\mathcal{I} - \alpha \mathcal{G})\mathbf{x}_n$ that converges to the fixed point of (4). In the linear measurement setting (1), this translates to

$$\mathbf{x}_{n+1} = \underbrace{(\mathcal{I} + \alpha \mathcal{F})^{-1}}_{\text{prox}_{\alpha} \phi}(\mathbf{x}_n - \underbrace{\alpha \lambda \mathcal{A}^H(\mathcal{A}(\mathbf{x}_n) - \mathbf{b})}_{\mathcal{G}(\mathbf{x}_n)}) \quad (5)$$

Here, $\text{prox}_{\alpha} \phi$ is the proximal operator of ϕ .

A. Plug and play methods

The steepest descent update $\mathbf{z}_n = \mathbf{x}_n - \alpha \lambda \mathcal{A}^H(\mathcal{A}(\mathbf{x}_n) - \mathbf{b})$ improves the data consistency, while the proximal mapping $\mathbf{x}_{n+1} = (\text{prox}_{\alpha} \phi)(\mathbf{z}_n)$ in (5) can be viewed as *denoising* the current solution $\mathbf{x}_n - \alpha \lambda \mathcal{A}^H(\mathcal{A}(\mathbf{x}_n) - \mathbf{b})$, thus moving the iterate towards the maximum of prior $p(\mathbf{x})$. Plug and play methods replace the proximal mapping with off-the-shelf or CNN denoisers \mathcal{P}_{θ} [6], [12], [15], [23]:

$$\mathbf{x}_{n+1} = \mathcal{P}_{\theta}(\mathbf{x}_n - \alpha \lambda \mathcal{A}^H(\mathcal{A}(\mathbf{x}_n) - \mathbf{b})) = \mathcal{T}(\mathbf{x}_n, \theta) \quad (6)$$

Here, θ denotes the learnable parameters.

There are PnP algorithms that use different optimization algorithms (e.g., ADMM, PG) with convergence guarantees to the fixed point $\mathbf{x}^* = \mathcal{P}_{\theta}(\mathbf{x}^* - \mathcal{G}(\mathbf{x}^*))$ [12]. The solutions obtained by these approaches often do not have a one-to-one correspondence to the MAP

setting in (3); they may be better understood from the consensus equilibrium setting [7]. See [12] for a detailed review of the PnP framework and associated convergence guarantees.

B. Unrolled optimization

Unrolled optimization schemes [13], [14], [24] aim to learn the CNN parameters that offer improved reconstruction for a specific sampling operator \mathcal{A} . These schemes unroll a finite number of iterations in (6) to obtain a deep network with shared CNN blocks. The parameters θ of the CNN are optimized to minimize the loss $L = \sum_i \|\tilde{\mathbf{x}}_{\theta,i} - \mathbf{x}_i\|_2^2$, where \mathbf{x}_i are the ground truth images and $\tilde{\mathbf{x}}_{\theta,i}$ are the output of the deep network. The main challenge of this scheme is the high memory demand of the unrolled algorithm, especially in higher-dimensional (e.g., 3D, 2D + time) settings. As a result, the iterations are often not run until convergence. While fewer (e.g., 10) iterations/unrolls are usually sufficient to offer good performance in the model-based deep learning (MoDL) [14] setting, the network trained for a specified number of unrolling steps may not yield the best performance when used for inference with different numbers of unrolling steps.

C. Deep equilibrium models

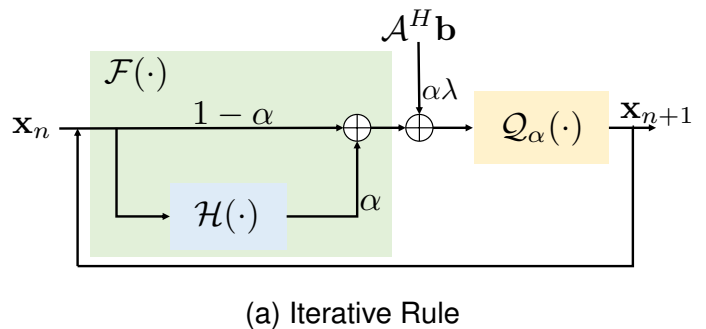
To overcome the challenges associated with unrolled schemes, [18] adapted the elegant DEQ approach introduced in [17]. Deep equilibrium models assume that the forward iterations in (6) are run until convergence to the fixed point \mathbf{x}^* that satisfies $\mathbf{x}^* = \mathcal{T}(\mathbf{x}^*, \theta)$. On applying the chain rule, $\partial_{\theta} \mathbf{x}^* = (\partial_{\mathbf{x}} \mathcal{T}|_{\mathbf{x}=\mathbf{x}^*}) \partial_{\theta} \mathbf{x}^* + \partial_{\theta} \mathcal{T}$, from which one obtains $\partial_{\theta} \mathbf{x}^* = (\mathcal{I} - \partial_{\mathbf{x}} \mathcal{T}|_{\mathbf{x}=\mathbf{x}^*})^{-1} (\partial_{\theta} \mathcal{T}|_{\mathbf{x}=\mathbf{x}^*})$. This relation can be substituted in $\partial_{\theta} \mathcal{C} = (\partial_{\theta} \mathbf{x}^*)^T (\partial_{\mathbf{x}^*} \mathcal{C})$ to obtain the partial derivative of the loss with respect to the CNN parameters:

$$\partial_{\theta} \mathcal{C} = (\partial_{\theta} \mathcal{T})^T (\mathcal{I} - \partial_{\mathbf{x}} \mathcal{T}|_{\mathbf{x}=\mathbf{x}^*})^{-1} (\partial_{\mathbf{x}^*} \mathcal{C})$$

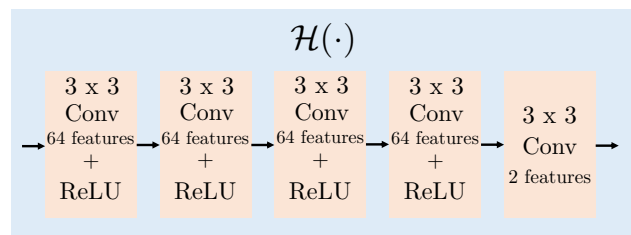
The above equation is solved using fixed-point iterations [17], [18] with just one physical layer. A requirement for the DEQ approach to work is the convergence of the forward and backward propagation steps. The convergence results in [10], [18] show that ADMM and PG algorithms converge to fixed points when the data-consistency term is strongly convex and $\mathcal{P}_{\theta} - \mathcal{I}$ is ϵ -Lipschitz, where ϵ depends on the algorithm parameters. The strict convexity of the data-consistency term is violated in the undersampled MRI setting.

III. MONOTONE OPERATOR LEARNING

As discussed in the introduction, the main goal of this work is to introduce DEQ algorithms that share the desirable properties of CS algorithms, including uniqueness of the solution, robustness to input perturbations, and guaranteed fast convergence. It is noted that current deep learning image reconstruction algorithms do not possess similar guarantees; there is a strong concern that they might be fragile to adversarial perturbations to the inputs [19]. In order to achieve the above goal, $\mathcal{F}(\mathbf{x})$ is constrained to be an m -monotone ($m > 0$) operator.



(a) Iterative Rule



(b) CNN architecture

Fig. 1. Figure (a) shows fixed-point iterative rule of proposed MOL algorithm from (9) and (b) shows the architecture of the 5-layer CNN $\mathcal{H}(\cdot)$ used in the experiments.

A. Proposed iterative algorithm

Current DEQ algorithms [18], [25] replace the proximal operator $\text{prox}_{\alpha} \phi$ with a CNN. By contrast, we model $\mathcal{F}(\mathbf{x}) = \nabla_{\mathbf{x}} \phi(\mathbf{x})$ with a monotone operator, parameterized using a CNN. We note that $\mathcal{F}(\mathbf{x}) = -\nabla_{\mathbf{x}} \log p_{\theta}(\mathbf{x})$ is termed as the score function of the prior probability density $p(\mathbf{x})$, which is a vector field pointing towards the maximum of the prior.

Using forward-backward splitting, we obtain the update rule:

$$\mathbf{x}_{n+1} = \underbrace{(\mathcal{I} + \alpha \mathcal{G})^{-1}}_{\text{prox}_{\alpha} \mathcal{D}} (\mathcal{I} - \alpha \mathcal{F})(\mathbf{x}_n) \quad (7)$$

As described above, fixed points of the above relation are equal to the fixed points of (3), for all $\alpha > 0$. In

the linear setting considered in (3), suppose we have $\mathbf{p} = (\text{prox}_\alpha \mathcal{D})(\mathbf{u}) = (\mathbf{I} + \alpha \mathcal{G})^{-1} \mathbf{u}$, which is the solution of $\mathbf{p} + \alpha \underbrace{(\lambda \mathcal{A}^H (\mathcal{A}(\mathbf{p}) - \mathbf{b}))}_{\mathcal{G}(\mathbf{p})} = \mathbf{u}$, or equivalently,

$$(\text{prox}_\alpha \mathcal{D})(\mathbf{u}) = \underbrace{(\mathcal{I} + \alpha \lambda \mathcal{A}^H \mathcal{A})^{-1}}_{\mathcal{Q}_\alpha} (\mathbf{u} + \alpha \lambda \mathcal{A}^H \mathbf{b}) \quad (8)$$

Combining with (7), we obtain the iterative algorithm:

$$\mathbf{x}_{n+1} = \underbrace{\mathcal{Q}_\alpha (\mathcal{I} - \alpha \mathcal{F})}_{\mathcal{T}} \mathbf{x}_n + \underbrace{\alpha \lambda \mathcal{Q}_\alpha \mathcal{A}^H \mathbf{b}}_{\mathcal{Z}} \quad (9)$$

When $\alpha = 1$, the fixed-point algorithm in the iterative rule in (9) can be rewritten as

$$\mathbf{x}_{n+1} = (\mathcal{I} + \lambda \mathcal{A}^H \mathcal{A})^{-1} (\mathcal{H}(\mathbf{x}_n) + \lambda \mathcal{A}^H \mathbf{b}), \quad (10)$$

where \mathcal{H} is a *denoiser*. It is shown in the next section that this approach converges to the unique fixed point of (4), denoted by $\mathbf{x}^*(\mathbf{b})$.

The above update rule is the fixed-point iteration approach in regularization by denoising (RED) [8] and the algorithm in MoDL [14]. Model-based deep learning trained \mathcal{H} by unrolling the iterative algorithm with a fixed number of iterations; it did not require the iterative rule to converge. By contrast, RED relied on pre-trained denoisers, which were used during inference time by iterating to convergence. The update rule in (9) can be viewed as a damped version of MoDL or fixed-point RED algorithm. As will be seen in our analysis later, the use of the damping factor $\alpha < 1$ enables us to relax the constraints on the CNN network \mathcal{H} that are needed for convergence, which will translate to improved representation power and performance.

B. Monotone operators and uniqueness of fixed point

Assumption: The operator $\mathcal{F} : \mathbb{C}^M \rightarrow \mathbb{C}^M$ is m -monotone if:

$$\langle \mathbf{x} - \mathbf{y}, \mathcal{F}(\mathbf{x}) - \mathcal{F}(\mathbf{y}) \rangle \geq m \|\mathbf{x} - \mathbf{y}\|_2^2, \quad m > 0. \quad (11)$$

for all $\mathbf{x}, \mathbf{y} \in \mathbb{C}^M$. Monotone operators enjoy several desirable properties and have been carefully studied in the context of convex optimization algorithms [26], mainly due to its following relation with convex priors.

Lemma III.1. [9], [11] *Let $\phi : \mathbb{C}^M \rightarrow \mathbb{R}_+$ be a proper, continuously differentiable, strongly convex function with $m > 0$. Then $F = \nabla \phi$ is an m -monotone operator.*

While derivatives of convex priors are monotone, the converse is not true in general. Our results show that the parameter m plays an important role in the convergence, uniqueness, and robustness of the algorithm

to perturbations. In the CS setting, \mathcal{A} often has a large null space, and hence the data-consistency term is not strictly convex. In this setting, many of the current PnP formulations do not have guarantees on the uniqueness of the fixed points. The following result shows that constraining \mathcal{F} to be m -monotone is sufficient to ensure the uniqueness of the fixed point of (4).

Proposition III.2. *The fixed point of (4) is unique for a specific \mathbf{b} , when \mathcal{F} is m -monotone with $m > 0$.*

The proof is provided in the appendix. While the above results can guarantee uniqueness, it is not useful unless there are efficient ways to represent and learn monotone operators. A parametric one-layer neural network, which is guaranteed to be monotone, was introduced in [27]. Unfortunately, this model lacks representation power in our setting. In the following results, it is shown that monotone operators can be represented efficiently using a residual neural network.

Proposition III.3. *$\mathcal{F} : \mathbb{C}^M \rightarrow \mathbb{C}^M$ is m -monotone if it can be represented as a residual operator $\mathcal{F} = \mathcal{I} - \mathcal{H}$, where $\mathcal{H} : \mathbb{C}^M \rightarrow \mathbb{C}^M$ has a Lipschitz constant of $(1 - m) > 0$. The Lipschitz constant of \mathcal{F} is $2 - m$:*

$$\|\mathcal{F}(\mathbf{x}) - \mathcal{F}(\mathbf{y})\|_2^2 \leq (2 - m) \|\mathbf{x} - \mathbf{y}\|_2^2. \quad (12)$$

This result allows us to construct a monotone operator as a residual CNN, involving a contractive network \mathcal{H} .

C. Monotonicity using Lipschitz regularization

A common approach to constrain a CNN to be contractive is spectral normalization of each layer of the CNN [10], [18]. While this approach can guarantee \mathcal{H} to be a contraction, the product of the Lipschitz constants of the individual layers is a conservative estimate of the Lipschitz constant of the network. In our experience, this approach results in networks with low capacity, which translates to lower performance. Another challenge with the spectral normalization approach is that it restricts the type of networks that can be used; architectures with skip connections cannot be used with this strategy.

To overcome the above challenges, we use the Lipschitz regularization strategy in [28]. The estimation of the Lipschitz constant of \mathcal{F} is posed as a maximization problem [28]:

$$L[\mathcal{H}] = \max_{\mathbf{x} \in S} \sup_{\boldsymbol{\eta}} \underbrace{\frac{\|\mathcal{H}(\mathbf{x} + \boldsymbol{\eta}) - \mathcal{H}(\mathbf{x})\|_2^2}{\|\boldsymbol{\eta}\|_2^2}}_{l_{\mathcal{H}}[\mathbf{x}]} \quad (13)$$

Here, $\boldsymbol{\eta}$ is a perturbation, and S is the set of training data samples.

In the supervised learning setting, we propose to minimize

$$\mathcal{C} = \sum_{i=0}^{N_t} \left(\underbrace{\|\mathbf{x}^*(\mathbf{b}_i) - \mathbf{x}_i\|_2^2}_{\text{MSE Loss}} + \beta \underbrace{l_{\mathcal{H}}[\mathbf{x}^*(\mathbf{b}_i)]}_{\text{Lipschitz Loss}} \right). \quad (14)$$

Here, $\mathbf{x}^*(\mathbf{b})$ is the fixed point of (4), while $\mathbf{x}_i; i = 0, \dots, N_t$ and $\mathbf{b}_i, i = 0, \dots, N_t$ are the ground truth images in the training dataset and their undersampled measurements, respectively. β is a regularization parameter that is used to control the Lipschitz constant of \mathcal{H} . For implementation purposes, we evaluate $l_{\mathcal{H}}[\mathbf{x}]$ for each of the training examples using steepest ascent; in particular, we initialize with a small vector δ and use steepest ascent to determine the δ that maximizes $l_{\mathcal{H}}[\mathbf{x}]$. The supervised training thus amounts to a min-max optimization scheme, where the criterion that is minimized at each iteration is derived using a maximization algorithm.

IV. THEORETICAL ANALYSIS

The monotone nature of \mathcal{F} allows us to characterize the fixed point of the iterative algorithm $\mathbf{x}_{n+1} = \mathcal{T}(\mathbf{x}_n) + \mathbf{z}$ in (9). In particular, we will now analyze the convergence and the robustness of the solution to input perturbations.

A. Convergence of the algorithm to a fixed point

Assuming that \mathcal{F} is m -monotone, we have the following results.

Lemma IV.1. *Let $\mathcal{F} : \mathbb{C}^M \rightarrow \mathbb{C}^M$ be an m -monotone operator. Then, the operator $\mathcal{R} = (\mathcal{I} - \alpha\mathcal{F})$ has a Lipschitz constant of*

$$L[\mathcal{R}] = \sqrt{1 + \alpha^2(2 - m)^2 + 2\alpha m}. \quad (15)$$

From the above relation, we note that \mathcal{R} is a contraction (i.e., $L[\mathcal{R}] < 1$) when the damping factor α satisfies

$$\alpha < \frac{2m}{(2 - m)^2}. \quad (16)$$

When $\mathcal{A}^H\mathcal{A}$ is full-rank, $\mathcal{Q}_\alpha = (\mathcal{I} + \alpha\lambda\mathcal{A}^H\mathcal{A})^{-1}$ is a contraction. However, in the CS setting, the Lipschitz constant of \mathcal{Q}_α is 1. The algorithm specified by (9) converges to the fixed point of (4) because the composition $\mathcal{Q}_\alpha \circ \mathcal{T}$ is a contraction, assuming (16), as shown in the result below.

Proposition IV.2. *Consider the algorithm specified by (9), where \mathcal{F} is an m -monotone operator. Assume that (9) has a fixed point specified by $\mathbf{x}^*(\mathbf{b})$. Then,*

$$\|\mathbf{x}_n - \mathbf{x}^*(\mathbf{b})\|_2 \leq (L_{\mathcal{T}})^n \|\mathbf{x}_0 - \mathbf{x}^*(\mathbf{b})\|_2, \quad (17)$$

where $L_{\mathcal{T}} = \frac{1}{(1 + \lambda\mu_{\min})} L[\mathcal{R}]$. Here, μ_{\min} is the minimum eigenvalue of $\mathcal{A}^H\mathcal{A}$ and $L[\mathcal{R}]$ is specified by (15).

We note that \mathcal{T} being a contraction translates to geometric convergence with a factor of $L[\mathcal{T}]$; this is faster than the sublinear convergence rates [9], [11] available for ISTA and ADMM in the CS setting ($\mu_{\min} = 0$).

Setting $\alpha = 1$ in (16), we see that the algorithm will converge if $L[\mathcal{R}] < 1$, or equivalently,

$$m \geq 3 - \sqrt{5} = 0.76 \quad (18)$$

or $L_{\mathcal{H}} < 0.24$; this severely restricts the capacity of \mathcal{H} , which translates to poor performance. The damping factor $\alpha < 1$ allows us to increase $L_{\mathcal{H}}$ while still obtaining algorithms that converge. For instance, if we choose $L_{\mathcal{H}} = 0.9$, we have $m = 0.1$; from (16), the algorithm will converge if $\alpha < 0.05$.

B. Robustness of the solution to input perturbation

As discussed above, a challenge with current deep learning algorithms is their sensitivity to input perturbations. The following result shows that the robustness of the results are dependent on m .

Proposition IV.3. *Consider \mathbf{z}_1 and \mathbf{z}_2 to be measurements with $\delta = \mathbf{z}_2 - \mathbf{z}_1$ as the perturbation. Let the corresponding outputs of the MOL algorithm be $\mathbf{x}^*(\mathbf{z}_1)$ and $\mathbf{x}^*(\mathbf{z}_2)$, respectively, with $\Delta = \mathbf{x}^*(\mathbf{z}_2) - \mathbf{x}^*(\mathbf{z}_1)$ as the output perturbation,*

$$\|\Delta\|_2 \leq \frac{\alpha\lambda}{1 - \sqrt{1 - 2\alpha m + \alpha^2(2 - m)^2}} \|\delta\|_2. \quad (19)$$

The above relation is complex to understand intuitively. Setting $\alpha \rightarrow 0$, the relation simplifies to

$$\|\Delta^*\|_2 = \lim_{n \rightarrow \infty} \|\Delta_n\|_2 \leq \frac{\lambda}{m} \|\delta\|_2$$

These relations show that the robustness of the algorithm is fundamentally related to m ; a higher value of m translates to a more robust algorithm. The Lipschitz constant $l[\mathcal{H}] = 1 - m$. We need to choose a network with a lower Lipschitz constant, and hence a lower representation power, to make the resulting algorithm more robust to perturbations. There is a trade-off between robustness and performance of the algorithm, controlled by either the parameter m or the Lipschitz constant $l[\mathcal{H}]$.

V. IMPLEMENTATION DETAILS

A. Datasets

We used the 2D multi-coil brain data from the publicly available Calgary-Campinas Public (CCP) Dataset [29].

The dataset consists of twelve-coil T1-weighted brain data from 117 healthy subjects, collected on a 3.0 Tesla MRI scanner. The scan parameters are: TR (repetition time)/TE (echo time)/TI (inversion time) = 6.3 ms / 2.6 ms / 650 ms or TR/TE/TI = 7.4 ms / 3.1 ms / 400 ms. Matrix sizes are 256 x 208 x 170/180 with 256, 208 and 170/180 being the readout, phase encoding, and slice encoding directions, respectively. For the experiments, we choose subjects with fully sampled data (67 out of 117) and split them into training (45), validation (2), and testing (20) sets. The data is retrospectively undersampled along the phase and slice encoding directions using a 4-fold 2D non-uniform variable-density mask.

To determine the utility of the algorithm in the 2D+time setting, we used the multi-coil cardiac data from the open-source OCMR Dataset [30]. It is noted that such 3D datasets are challenging to solve using the traditional MoDL [14] framework due to its high memory demand. The scans are obtained either from a 1.5 Tesla or a 3.0 Tesla scanner. We chose data from 1.5 Tesla scans for our experiments. It consists of a series of short-axis, long-axis, or 4-chamber views. The dataset split is 15, 2, and 8 subjects for training, validation, and testing, respectively. Since the data is a 2D multi-slice acquisition, we retrospectively undersample it using a 1D non-uniform variable-density mask along the phase encode direction.

B. Quality evaluation metric

The reconstruction results are quantitatively evaluated in terms of the Structural Similarity Index (SSIM) [31] and the peak signal-to-noise ratio (PSNR). The PSNR of a predicted image \mathbf{x}_p with respect to its corresponding fully sampled ground truth image \mathbf{x}_g is defined as

$$\text{PSNR (dB)} = 20 \cdot \log_{10} \left(\frac{\max(\mathbf{x}_g)}{\|\mathbf{x}_p - \mathbf{x}_g\|_2} \right), \quad (20)$$

where $\max(\cdot)$ is the maximum pixel value of the image.

C. State-of-the-art methods for comparison

We compare the proposed MOL algorithm against SENSE [32], MoDL [14], ADMM-Net [16], DE-GRAD [18], and UNET [33] for experiments on CCP brain data. SENSE is a CS-based approach that uses a forward model consisting of coil sensitivity weighting and undersampled Fourier transform. MoDL and ADMM-Net are unrolled deep learning algorithms, which alternate between the SENSE-based data consistency (DC) step and the CNN-based denoising step. Both approaches are trained in an end-to-end fashion for 10 iterations. DE-GRAD is a deep equilibrium network, where we use

spectral normalization as described in [18]. UNET is a direct inversion approach, which uses a CNN without any data-consistency steps.

We consider two versions of MOL: MOL-SN, which relies on spectral normalization during training to constrain the Lipschitz constant of the overall network, and MOL-LR, which consists of an additional loss term computing the Lipschitz constant of the CNN. For 3D experiments on OCMR cardiac data, we compare a 3D version of MOL-LR (with 3D convolutions) against the 2D MoDL.

D. Architecture of the CNNs and training details

The MOL architecture is shown in Fig. 1. In our 3D experiments, the CNN \mathcal{H} consists of five 2D convolution layers, each followed by rectified linear unit (ReLU) non-linearity, except for the last layer. The convolution layers consist of 64 3x3 filters. The parameter λ in (9), weighing the data-consistency term, is kept trainable. A SENSE reconstruction with $\lambda = 100$ is performed initially on the undersampled image $\mathcal{A}^H \mathbf{b}$ to initialize the MOL network as \mathbf{x}_0 . A similar approach is used for the other deep learning networks (MoDL, ADMM-Net, UNET) to ensure fair comparisons. We share the CNN weights across the iterations for all the unrolled deep learning algorithms (MoDL, ADMM-Net). We chose the size of the UNET to be roughly similar to the five-layer CNNs used in other algorithms, for a fair comparison. In 3D experiments, a five-layer CNN is chosen; it is similar to the 2D case, with the exception of 3D convolution layers instead of 2D. An $\alpha = 0.055$ is chosen for MOL algorithms in all cases.

All the trainings are performed on a 16 GB NVIDIA P100 GPU. The CNN weights are Xavier initialized and trained using an Adam optimizer for 200 epochs. The learning rates for updating CNN weights and λ are chosen empirically as 10^{-4} and 1.0, respectively. MoDL and ADMM-Net are unrolled for 10 iterations; MOL, on the other hand, consumes memory equivalent to a single iteration.

VI. EXPERIMENTS AND RESULTS

A set of experiments has been conducted on brain data from the CCP [29] to compare the proposed framework against state-of-the-art methods. Another experiment to show the benefit of the reduced memory demand of our proposed approach is performed on the cardiac CINE data from the OCMR [30].

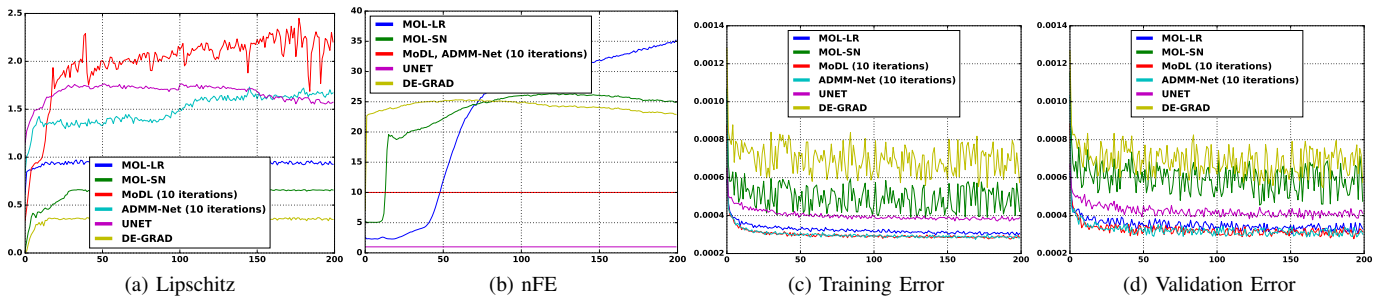


Fig. 2. Comparison of MOL with Lipschitz unconstrained algorithms and other DEQ frameworks. Graphs are plotted with respect to epochs during training. (a) shows the evolution of the Lipschitz constant of the CNN. (b) plots the number of iterations used in the algorithm. For MoDL and ADMM-Net, we have 10 unrolls, and UNET consists of a single CNN. The DEQ forward and backward algorithms are run until the difference between the subsequent terms is 0.05%. We note that MOL-LR requires more forward iterations to converge compared to MOL-SN, mainly because of the higher Lipschitz constant of \mathcal{H} . The plots in (c) and (d) are the training and validation errors in each case. MOL-SN has significantly higher errors due to spectral normalization of weights restricting the representation power. MOL-LR achieves error comparable to the unrolled methods.

A. Characterization of the models

In Fig. 2, we show the characteristics of different models during training. We tuned the β parameter in (14) such that the Lipschitz constant of \mathcal{H} computed using (13) remains less than 1, which ensures convergence with the right choice of α . MOL-SN involves spectral normalization of the weights, which is found to be a more conservative bound; the computed Lipschitz constant of \mathcal{H} stays around 0.7, which translates to lower performance or, equivalently, higher error. By contrast, the unrolled MoDL and ADMM-Net, as well as UNET, have no Lipschitz constraints and, therefore, have more flexibility in CNN weight updates. It is observed that the Lipschitz constants of these networks often exceed 1.

Plot Fig. 2.(b) shows the number of CNN function evaluations (nFE) or iterations of the algorithm in (9) needed to converge to the fixed point with a precision of 10^{-4} . As expected, MOL-SN and DE-GRAD, which have a lower Lipschitz constants and hence higher m , converge more rapidly than MOL-LR, which has a lower m . The plots (c) and (d) show training and validation errors in each case. It is noted that MOL-LR has marginally higher training and validation errors compared to MoDL and ADMM-Net, which are unrolled algorithms. We attribute the higher errors to the lower Lipschitz constants of the corresponding \mathcal{H} networks. MOL-SN and DE-GRAD, which use spectral normalization, have even higher errors compared to MOL-LR due to even lower Lipschitz constant. These results show that there is a trade-off between performance and computational complexity, governed by m ; a higher m translates to a faster algorithm but is associated with lower performance resulting from the limited capacity of the resulting networks.

B. Performance comparison

Four-fold Accelerated Brain MRI Recovery		
Methods	PSNR	SSIM
SENSE	31.13	0.982
MOL-SN	33.05	0.986
DE-GRAD	32.84	0.985
MOL-LR	36.56	0.992
MoDL	36.89	0.993
ADMM-Net	36.77	0.993
UNET	34.69	0.986

TABLE I
QUANTITATIVE COMPARISONS ON 2D DATA.

The comparison of performance on the four-fold accelerated brain data is shown in Fig. 3 and Table I, respectively. Table I reports performance in terms of mean PSNR and SSIM on 20 subjects. The performance of MOL-LR is comparable to 10-iteration MoDL and ADMM-Net. The marginal drop in performance can be attributed to the lower representation power resulting from the Lipschitz constraints. It is observed from Fig. 2.(a) that the reduction in performance is higher for MOL-SN because of the lower Lipschitz constant of \mathcal{H} . The performance of the UNET is lower than that of the unrolled algorithms MoDL, ADMM-Net, and MOL-LR. Similar trends are observed in the quality of reconstructions shown in Fig. 3. The error images show higher errors in important brain regions with MOL-SN and UNET, while the error images from MOL-LR, MoDL, and ADMM-Net are comparable. These comparisons show that the Lipschitz regularization strategy offers better performance than spectral normalization.

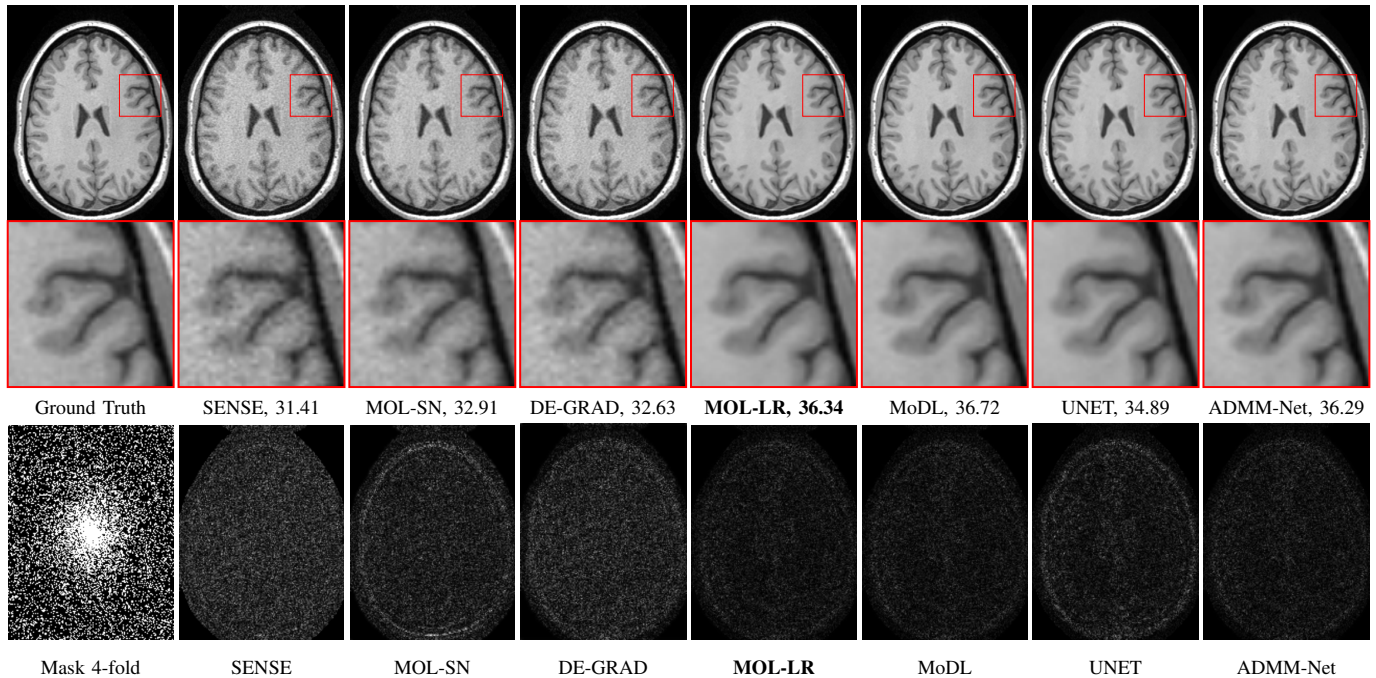


Fig. 3. Reconstruction results of 4x accelerated multi-channel brain data. PSNR (dB) values are reported for each case. The image in the first row and column was undersampled using a Cartesian 2D non-uniform variable-density mask as shown in the first column, second row. The top row shows reconstructions (magnitude images), while the bottom row shows corresponding error images. We note that the quality of the **MOL-LR** reconstructions is comparable to unrolled methods MoDL and ADMM-Net. MOL-SN and DE-GRAD show significantly lower performance due to spectral normalization of weights, resulting in stricter bounds on the Lipschitz constant of its CNN, thus restricting the representation power.

C. Robustness

We compare the robustness of the networks on four-fold accelerated brain data in Fig. 4 and Fig. 5. Specifically, we study the change in output with respect to perturbations to input to determine the stability of the models. The perturbations are added to the undersampled measurements \mathbf{b} .

1) *Worst-case (adversarial) perturbations:* We determine the worst-case perturbation γ with energy of ϵ by solving the following optimization problem:

$$s_\epsilon = \sup_{\gamma: \|\gamma\|_2 < \epsilon} \|\mathbf{x}^*(\mathbf{b} + \gamma) - \mathbf{x}^*(\mathbf{b})\|_2^2. \quad (21)$$

The above optimization problem is solved using multiple gradient ascent steps, each followed by renormalizing γ to satisfy the constraint $\|\gamma\|_2 < \epsilon$.

The perturbed output $\mathbf{x}^*(\mathbf{b} + \gamma)$ corresponding to an input perturbation of $\epsilon = 1\%$ noise is shown in the second row of Fig. 4. The top row shows that the performance of MOL-LR is comparable to MoDL and ADMM-net in the noiseless setting, which is consistent with the findings in Table I. A significant drop in PSNR (≈ 5 -6 dB) is observed in MoDL, ADMM-Net, and UNET reconstructions with increasing value

of ϵ . Note that these models were trained with no constraints. By contrast, the MOL-LR scheme is relatively less vulnerable to the perturbations. MOL-SN and DE-GRAD, which have a smaller Lipschitz constants for \mathcal{H} than MOL-LR, are least affected by the perturbations. In particular, MoDL, ADMM-Net, and UNET show strong edge-like artifacts, whereas the Lipschitz regularized schemes exhibit more graceful deterioration. The third row shows that the approaches without Lipschitz constraints completely break down with 5% noise. The comparison of the models on all of the test data is shown in Fig. 5. (a). The models without Lipschitz constraints (MoDL, ADMM-Net, UNET) exhibit a drastic drop with $\epsilon > 0.01$, whereas SENSE, MOL-LR, and MOL-SN have an approximately linear drop. MOL-SN and DE-GRAD (red & black curves) are the flattest, which can be explained with the smaller Lipschitz constant.

2) *Gaussian perturbations:* We now study the sensitivity of the models to 1% Gaussian perturbations. The output reconstructions obtained in each case are shown in the bottom row of Fig. 4. We note that the drop in performance of MOL approaches and SENSE is consistent with the worst-case setting in the second

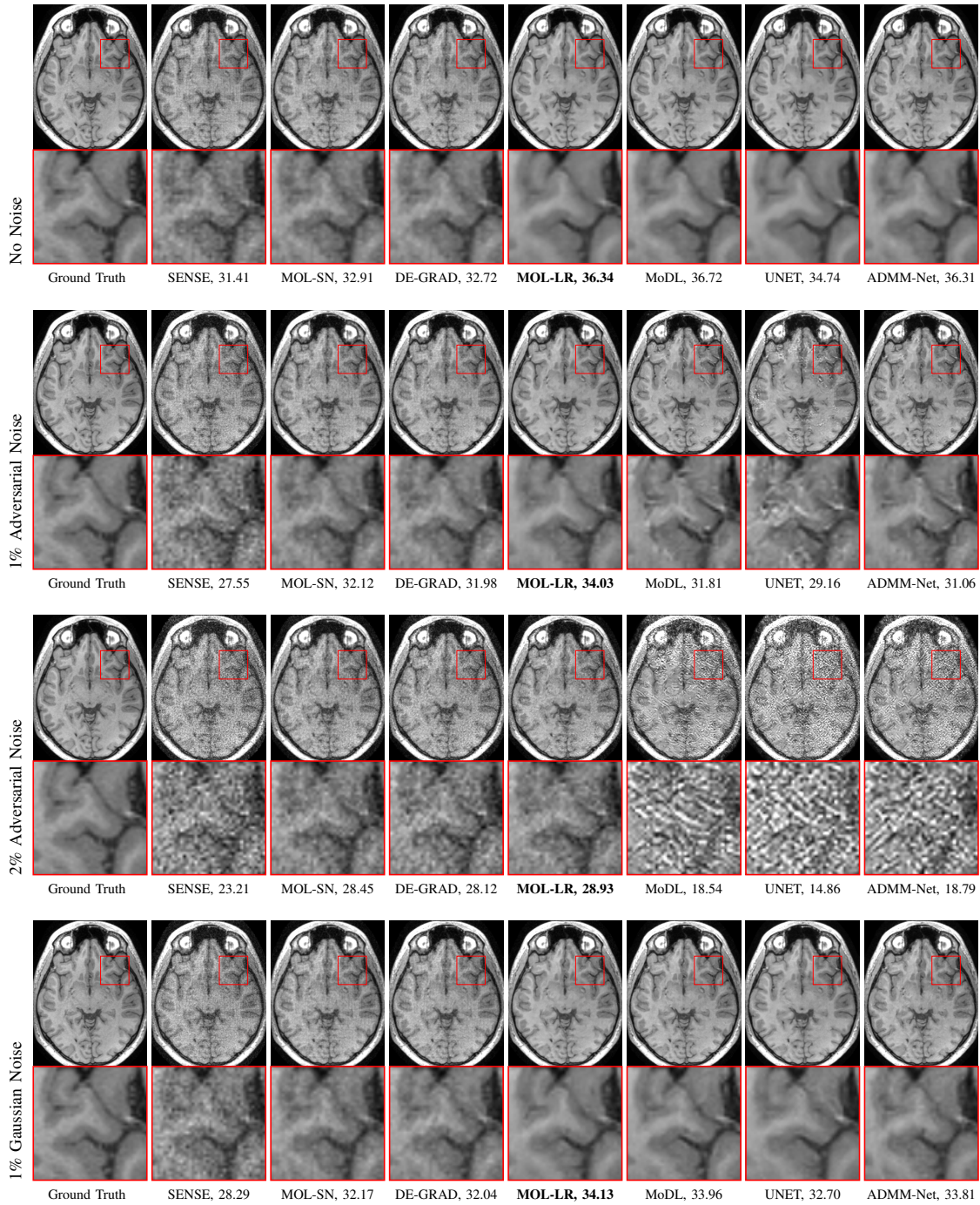


Fig. 4. Sensitivity of the algorithms to input perturbations: The rows correspond to reconstructed magnitude results of 4x accelerated multi-channel brain data for no noise, Gaussian, and worst-case (adversarial) noise, respectively. The PSNR (dB) values are reported for each case. The data was undersampled using a Cartesian 2D non-uniform variable-density mask. The top row shows reconstructions with no added noise, the second and third rows show 1% and 2% adversarial noise, respectively, and the fourth row shows 1% Gaussian noise. The inputs of the trained networks are corrupted with worst-case (second and third rows) or Gaussian (last row) noise. We note a sharp drop in PSNR for the unrolled algorithms (MoDL, ADMM-Net) and UNET with worst-case perturbations, which indicates fragility to adversarial noise. Significant artifacts are visible in the reconstructions. By contrast, the Lipschitz-constrained MOL algorithms and DE-GRAD algorithms exhibit a lower drop in PSNR, indicating graceful deterioration in performance. The performance of all algorithms remains less affected in each case by Gaussian noise. We note that the performance of the Lipschitz-constrained algorithms is similar for Gaussian and worst-case noise with the same variance.

row. By contrast, the Lipschitz-unconstrained schemes (MoDL, ADMM-Net, and UNET) offer comparable per-

formance to the worst-case setting. These results agree with previous studies (e.g., [14]) that deep networks are

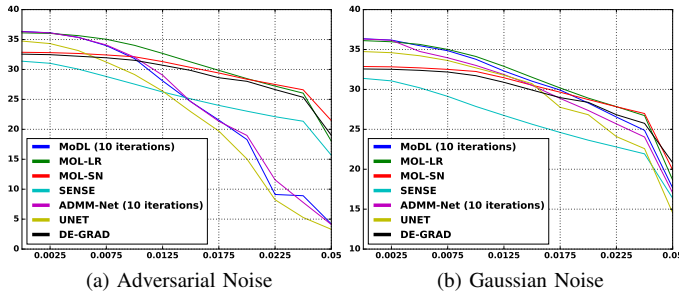


Fig. 5. Quantitative comparison of the robustness of different algorithms to adversarial and Gaussian noise. (a) shows a plot between PSNR and percentage of adversarial noise, and (b) shows a similar plot for Gaussian noise. The x-axis represents epsilon (factor) of noise added. From (a), it is observed that for models trained without any Lipschitz constraints (MoDL, ADMM-Net, UNET), PSNR drops significantly at around 1% adversarial noise, compared to Lipschitz-constrained models where performance decreases at a slower pace. In the case of Gaussian noise in (b), all the models have an almost linear decrease in performance. These results show that the worst-case performance of the MOL schemes is quite comparable to the Gaussian noise setting. By contrast, the unconstrained schemes exhibit instability in the presence of worst-case adversarial perturbations.

robust to Gaussian noise perturbations. From plot (b) in Fig. 5, it is observed that all the models have a linear drop at a similar rate with increase in Gaussian noise percentage (ϵ). These experiments confirm that there is no major difference in performance between the Gaussian and worst-case perturbations for Lipschitz-constrained models. However, the models trained without Lipschitz constraints are considerably more vulnerable to worst-case/adversarial perturbations.

2D vs 3D Cardiac CINE MRI Recovery				
Acceleration	4x		6x	
	PSNR	SSIM	PSNR	SSIM
Zero-filled	25.25	0.764	23.64	0.712
MoDL 2D	38.21	0.975	36.94	0.959
MOL-LR 3D	40.68	0.988	39.16	0.976

TABLE II
QUANTITATIVE COMPARISONS ON 2D+TIME CINE DATA.

D. Illustration in high dimensional settings

MOL requires only one physical layer to evaluate the forward and backward propagations; the memory demand of MOL-LR is 10x times smaller than that of the unrolled networks with ten iterations. Our experiments show that MOL-LR achieves performance similar to unrolled algorithms at a much lower memory footprint, which makes it an attractive option for large-scale problems. In this section, we illustrate the applicability of the MOL frameworks to such problems. The joint

recovery of 2D+time data using different undersampling patterns for each time point can capitalize on the strong redundancy between the time frames. However, it is challenging to use conventional unrolled optimization algorithms because of the high memory demand. We compare the performance of a 3D (2D+time) version of MOL-LR against a 2D MoDL (10 iterations) for recovery of time series of cardiac CINE MRI.

The reconstructions results for six-fold and four-fold accelerated CINE MRI recovery are shown in Fig. 6.(a) and Fig. 6.(b), respectively. The top two rows correspond to the diastole and systole phases, respectively. The bottom row corresponds to the time series. It is observed from the top two rows that the 2D+time MOL-LR approach is able to minimize spatial blurring compared to the 2D MoDL approach. The frame-to-frame changes in aliasing artifacts can also be appreciated from the time plots. Table II displays the mean PSNR and SSIM over eight test subjects. MOL-LR 3D outperforms MoDL 2D in terms of PSNR (by ≈ 2 dB) and SSIM at both the acceleration factors.

VII. CONCLUSION

We introduced a deep monotone operator learning framework for model-based deep learning for inverse problems in imaging. The proposed approach learns a monotone CNN in a deep equilibrium algorithm. The monotone constraint on the CNN allows us to introduce guarantees on the uniqueness of the solution, rapid convergence, and stability of the solution to input perturbations. These are desirable properties enjoyed by CS algorithms. The proposed approach enforces monotonicity by expressing it as a residual CNN, where the Lipschitz constant of the CNN block is less than unity. We use a Lipschitz regularization scheme to control the Lipschitz constant, which is less constrained than the spectral normalization used by current DEQ formulations. Our experiments show that the regularization strategy offers improved performance. A benefit of the Lipschitz regularization scheme is its applicability to any deep learning network architecture. The DEQ formulation enables forward and backward propagation using a single physical layer, thus significantly reducing the memory demand.

We validate the framework for parallel MRI recovery setting. The results show that the proposed MOL framework provides similar performance to unrolled MoDL algorithms, but with significantly reduced memory. More importantly, we observed that the framework was more robust to worst-case input perturbations than unrolled approaches such as MoDL and ADMM; the worst-case

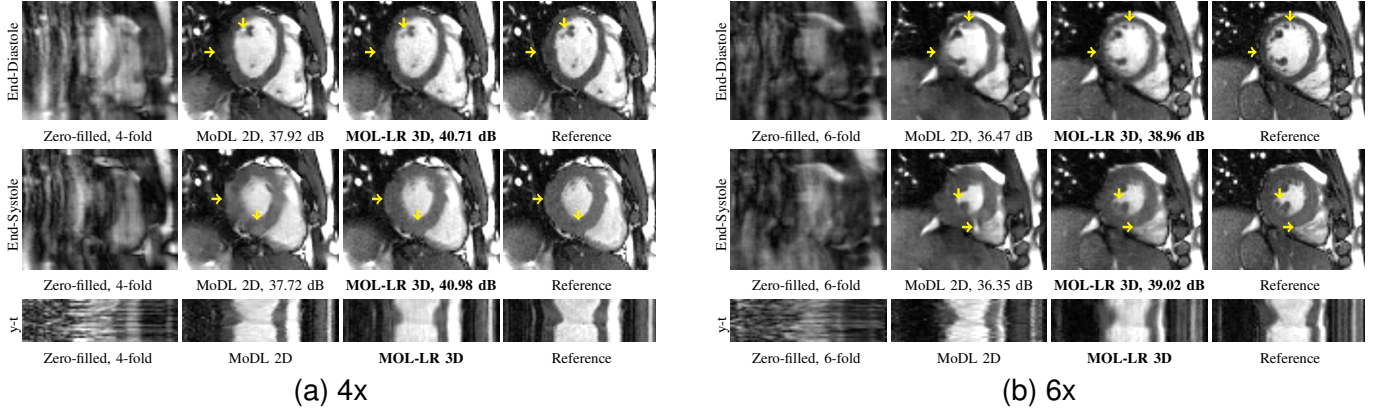


Fig. 6. MOL recovery of 2D+time cine data at 4x and 6x accelerations. The PSNR (dB) values are reported for each case. The data is retrospectively undersampled using a Poisson density sampling pattern. For both figures (a) and (b), the top and bottom rows correspond to the diastole and systole phases, respectively. For MoDL 2D and MOL-LR 3D, reconstructions (magnitude images) are shown. MoDL 2D has more errors in the boundary of the myocardium compared to MOL-LR 3D as pointed by the yellow arrows. MoDL 2D reconstructs images in the spatial domain only, whereas MOL-LR 3D exploits redundancies in the additional temporal domain, leading to lower errors. The short axis cut looks sharper for MOL-LR 3D, and it preserves the wall thickness better.

performance of the proposed approach was comparable to the performance degradation in the presence of Gaussian noise. The memory efficiency of the proposed scheme enabled us to apply it to a larger-scale (2D+time) problem, which is not usually possible with MoDL. The MOL-LR 3D reconstructions were found to be of superior quality when compared to 2D MoDL.

VIII. APPENDIX

A. Proof of Lemma III.1

Proof. We have

$$f(y) \geq f(x) + F(x)^T(y - x) + \frac{m}{2}\|y - x\|_2^2 \quad (22)$$

$$f(x) \geq f(y) + F(y)^T(x - y) + \frac{m}{2}\|x - y\|_2^2. \quad (23)$$

Adding the two relations, we get

$$\langle F(y) - F(x), (x - y) \rangle \geq m\|x - y\|_2^2. \quad (24)$$

□

B. Proof of Proposition III.2

Proof. Assume that there exist two fixed points $\mathbf{x} \neq \mathbf{y}$ for a specific \mathbf{b} :

$$\lambda \mathcal{A}^H(\mathcal{A}(\mathbf{x}) - \mathbf{b}) + \mathcal{F}(\mathbf{x}) = 0 \quad (25)$$

$$\lambda \mathcal{A}^H(\mathcal{A}(\mathbf{y}) - \mathbf{b}) + \mathcal{F}(\mathbf{y}) = 0 \quad (26)$$

which gives

$$\mathbf{z} = \lambda \mathcal{A}^H(\mathcal{A}(\mathbf{x} - \mathbf{y})) + \mathcal{F}(\mathbf{x}) - \mathcal{F}(\mathbf{y}) = \mathbf{0}. \quad (27)$$

Setting, $\mathbf{v} = \mathbf{x} - \mathbf{y}$, we consider

$$\begin{aligned} \langle \mathbf{z}, \mathbf{v} \rangle &= \underbrace{\langle \lambda \mathcal{A}^H \mathcal{A}(\mathbf{v}), \mathbf{v} \rangle}_{\geq \lambda \mu_{\min} \|\mathbf{v}\|_2^2} + \underbrace{\langle \mathcal{F}(\mathbf{x}) - \mathcal{F}(\mathbf{y}), \mathbf{v} \rangle}_{\geq m \|\mathbf{v}\|_2^2} \\ &\geq (\lambda \mu_{\min} + m) \|\mathbf{v}\|_2^2 \end{aligned}$$

where $\mu_{\min} \geq 0$ is the minimum eigenvalue of $\mathcal{A}^H \mathcal{A}$ operator and \mathcal{F} is m -monotone. The above relation is true only if $\mathbf{v} = \mathbf{0}$ or $\mathbf{z} \neq \mathbf{0}$. The first condition is true if $\mathbf{x} = \mathbf{y}$, while the second condition implies that (27) is not true. □

C. Proof of Proposition III.3

Proof. Let the Lipschitz constant of H is $1 - m$,

$$\|\mathcal{H}(\mathbf{x}) - \mathcal{H}(\mathbf{y})\|_2 \leq \underbrace{(1 - m)}_{\epsilon} \|\mathbf{x} - \mathbf{y}\|_2, \quad \epsilon > 0. \quad (28)$$

We consider the inner product,

$$\begin{aligned} &\langle \mathcal{F}(\mathbf{x}) - \mathcal{F}(\mathbf{y}), \mathbf{x} - \mathbf{y} \rangle \quad (29) \\ &= \langle (\mathcal{I} - \mathcal{H})\mathbf{x} - (\mathcal{I} - \mathcal{H})\mathbf{y}, \mathbf{x} - \mathbf{y} \rangle \\ &= \|\mathbf{x} - \mathbf{y}\|_2^2 - \langle \mathcal{H}(\mathbf{x}) - \mathcal{H}(\mathbf{y}), \mathbf{x} - \mathbf{y} \rangle. \end{aligned}$$

Using Cauchy Schwartz,

$-\|\mathbf{a}\|_2 \cdot \|\mathbf{b}\|_2 \leq \langle \mathbf{a}, \mathbf{b} \rangle \leq \|\mathbf{a}\|_2 \cdot \|\mathbf{b}\|_2$ and (28), we bound the second term as

$$-\epsilon \|\mathbf{x} - \mathbf{y}\|_2^2 \leq \langle \mathcal{H}(\mathbf{x}) - \mathcal{H}(\mathbf{y}), \mathbf{x} - \mathbf{y} \rangle \leq \epsilon \|\mathbf{x} - \mathbf{y}\|_2^2 \quad (30)$$

Combining with (29), we obtain

$$\begin{aligned} \underbrace{(1 - \epsilon) \|\mathbf{x} - \mathbf{y}\|_2^2}_m &\leq \langle \mathcal{F}(\mathbf{x}) - \mathcal{F}(\mathbf{y}), \mathbf{x} - \mathbf{y} \rangle \\ \langle \mathcal{F}(\mathbf{x}) - \mathcal{F}(\mathbf{y}), \mathbf{x} - \mathbf{y} \rangle &\leq \underbrace{(1 + \epsilon) \|\mathbf{x} - \mathbf{y}\|_2^2}_{2-m} \end{aligned}$$

This shows that \mathcal{F} is m -monotone and has a Lipschitz constant of $(1 + \epsilon)$. \square

D. Proof of Lemma IV.1

Proof. Using $\mathcal{R} = (\mathcal{I} - \alpha\mathcal{F})$,

$$\begin{aligned} \|\mathcal{R}(\mathbf{x}) - \mathcal{R}(\mathbf{y})\|_2^2 &= \|\mathbf{x} - \mathbf{y} - \alpha\mathcal{F}(\mathbf{x}) + \alpha\mathcal{F}(\mathbf{y})\|_2^2 \\ &= \|\mathbf{x} - \mathbf{y}\|_2^2 + \alpha^2 \|\mathcal{F}(\mathbf{x}) - \mathcal{F}(\mathbf{y})\|_2^2 \\ &\quad - 2\alpha \langle \mathbf{x} - \mathbf{y}, \mathcal{F}(\mathbf{x}) - \mathcal{F}(\mathbf{y}) \rangle. \end{aligned}$$

Using (12) for the second term and (11) for the last term, we obtain

$$\begin{aligned} \|\mathcal{R}(\mathbf{x}) - \mathcal{R}(\mathbf{y})\|_2 &\leq \|\mathbf{x} - \mathbf{y}\|_2 \sqrt{1 + \alpha^2(2 - m)^2 - 2\alpha m}, \\ \text{which shows that } L[\mathcal{R}] &= \sqrt{1 + \alpha^2(2 - m)^2 - 2\alpha m}. \end{aligned} \quad \square$$

E. Proof of Proposition IV.2

Proof. We first show that the operator \mathcal{T} in the iterative relation

$$\mathbf{x}_{n+1} = \mathcal{T}(\mathbf{x}_n) + \mathbf{z} \quad (31)$$

is a contraction. In particular, the Lipschitz constant of \mathcal{Q}_α is given by $L[\mathcal{Q}_\alpha] = \frac{1}{(1 + \lambda\mu_{\min})}$, where $\mu_{\min} \geq 0$ is the minimum eigenvalue of $\mathcal{A}^H \mathcal{A}$. Under the conditions of the theorem, the Lipschitz constant $L[\mathcal{I} - \alpha\mathcal{F}]$ is less than one. Combining the two, we have $L_{\mathcal{T}} < 1$. If \mathbf{x}^* is a fixed point, we have $\mathbf{x}^* = \mathcal{T}(\mathbf{x}^*) + \mathbf{z}$. We thus have

$$\begin{aligned} \|\mathbf{x}_n - \mathbf{x}^*\|_2 &= \|\mathcal{T}(\mathbf{x}_{n-1}) - \mathcal{T}(\mathbf{x}^*)\|_2 \\ &\leq L_{\mathcal{T}} \|\mathbf{x}_{n-1} - \mathbf{x}^*\|_2 \\ &\leq (L_{\mathcal{T}})^n \|\mathbf{x}_0 - \mathbf{x}^*\|_2, \end{aligned}$$

which implies that $\mathbf{x}_n \rightarrow \mathbf{x}^*$ as $n \rightarrow \infty$. \square

F. Proof of Proposition IV.3

Proof. Consider the iterative rule in (9),

$$\begin{aligned} \mathbf{x}_n &= \underbrace{\mathcal{Q}_\alpha(\mathcal{I} - \alpha\mathcal{F})}_{\mathcal{T}}(\mathbf{x}_{n-1}) + \alpha\lambda \underbrace{\mathcal{Q}_\alpha(\mathcal{A}^H \mathbf{b})}_{\mathbf{w}} \\ &= \mathcal{T}^2(\mathbf{x}_{n-2}) + (\mathcal{T} + I) \alpha\lambda \mathcal{Q}_\alpha(\mathbf{w}) \\ &= \mathcal{T}^n(\mathbf{x}_0) + (\mathcal{T}^{n-1} + \mathcal{T} + \dots + I) \alpha\lambda \mathcal{Q}_\alpha(\mathbf{w}) \end{aligned} \quad (32)$$

The Lipschitz bound of \mathcal{Q}_α is,

$$L_{\mathcal{Q}_\alpha} = \frac{1}{1 + \lambda\mu_{\min}}, \quad (33)$$

$$L_{\mathcal{T}} = L_{\mathcal{Q}_\alpha} \sqrt{1 + \alpha^2(2 - m)^2 - 2\alpha m}. \quad (34)$$

Consider \mathbf{z}_1 and \mathbf{z}_2 as two input measurements with $\boldsymbol{\delta} = \mathbf{z}_2 - \mathbf{z}_1$ as the perturbation in the input. Let the corresponding outputs be $\mathbf{x}_{1,n}$ and $\mathbf{x}_{2,n}$, respectively, with $\Delta_n = \mathbf{x}_{2,n} - \mathbf{x}_{1,n}$ as the perturbation in the output. Thus, the perturbation in the output can be written as

$$\begin{aligned} \|\Delta_n\|_2 &= \|\mathcal{T}(\mathbf{x}_{1,n-1}) - \mathcal{T}(\mathbf{x}_{2,n-1}) + \alpha\lambda \mathcal{Q}_\alpha(\boldsymbol{\delta})\|_2 \\ &\leq \|\mathcal{T}(\mathbf{x}_{1,n-1}) - \mathcal{T}(\mathbf{x}_{2,n-1})\|_2 + \alpha\lambda \|\mathcal{Q}_\alpha(\boldsymbol{\delta})\|_2 \\ &\leq L_{\mathcal{T}} \|\Delta_{n-1}\|_2 + \alpha\lambda L_{\mathcal{Q}_\alpha} \|\boldsymbol{\delta}\|_2 \end{aligned}$$

Using (32), we can expand the above relation as

$$\begin{aligned} \|\Delta_n\|_2 &\leq (L_{\mathcal{T}})^n \|\Delta_0\|_2 + \\ &\quad \alpha\lambda ((L_{\mathcal{T}})^{n-1} + (L_{\mathcal{T}})^{n-2} + \dots + 1) L_{\mathcal{Q}_\alpha} \|\boldsymbol{\delta}\|_2. \end{aligned}$$

When $L_{\mathcal{T}} < 1$, the first term vanishes, and we have

$$\lim_{n \rightarrow \infty} \|\Delta_n\|_2 \leq \frac{\alpha\lambda L_{\mathcal{Q}_\alpha}}{1 - L_{\mathcal{T}}} \|\boldsymbol{\delta}\|_2.$$

In CS setting, $\mu_{\min} = 0$ and therefore,

$$\lim_{n \rightarrow \infty} \|\Delta_n\|_2 \leq \frac{\alpha\lambda}{1 - \sqrt{1 + \alpha^2(2 - m)^2 - 2\alpha m}} \|\boldsymbol{\delta}\|_2. \quad (35) \quad \square$$

REFERENCES

- [1] J. A. Fessler, "Model-based image reconstruction for MRI," *IEEE signal processing magazine*, vol. 27, no. 4, pp. 81–89, 2010.
- [2] I. A. Elbakri and J. A. Fessler, "Statistical image reconstruction for polyenergetic X-ray computed tomography," *IEEE transactions on medical imaging*, vol. 21, no. 2, pp. 89–99, 2002.
- [3] J. Verhaeghe, D. Van De Ville, I. Khalidov, Y. D'Asseler, I. Lemahieu, and M. Unser, "Dynamic PET reconstruction using wavelet regularization with adapted basis functions," *IEEE Transactions on Medical Imaging*, vol. 27, no. 7, pp. 943–959, 2008.
- [4] F. Aguet, D. Van De Ville, and M. Unser, "Model-based 2.5-D deconvolution for extended depth of field in brightfield microscopy," *IEEE Transactions on Image Processing*, vol. 17, no. 7, pp. 1144–1153, 2008.
- [5] M. Lustig, D. Donoho, and J. M. Pauly, "Sparse MRI: The application of compressed sensing for rapid MR imaging," *Magnetic Resonance in Medicine: An Official Journal of the International Society for Magnetic Resonance in Medicine*, vol. 58, no. 6, pp. 1182–1195, 2007.
- [6] S. V. Venkatakrisnan, C. A. Bouman, and B. Wohlberg, "Plug-and-play priors for model based reconstruction," in *2013 IEEE Global Conference on Signal and Information Processing*. IEEE, 2013, pp. 945–948.

- [7] G. T. Buzzard, S. H. Chan, S. Sreehari, and C. A. Bouman, "Plug-and-play unplugged: Optimization-free reconstruction using consensus equilibrium," *SIAM Journal on Imaging Sciences*, vol. 11, no. 3, pp. 2001–2020, 2018.
- [8] Y. Romano, M. Elad, and P. Milanfar, "The little engine that could: Regularization by denoising (RED)," *SIAM Journal on Imaging Sciences*, vol. 10, no. 4, pp. 1804–1844, 2017.
- [9] Y. Sun, B. Wohlberg, and U. S. Kamilov, "An online plug-and-play algorithm for regularized image reconstruction," *IEEE Transactions on Computational Imaging*, vol. 5, no. 3, pp. 395–408, 2019.
- [10] E. Ryu, J. Liu, S. Wang, X. Chen, Z. Wang, and W. Yin, "Plug-and-play methods provably converge with properly trained denoisers," in *International Conference on Machine Learning*. PMLR, 2019, pp. 5546–5557.
- [11] Y. Sun, Z. Wu, X. Xu, B. Wohlberg, and U. S. Kamilov, "Scalable plug-and-play ADMM with convergence guarantees," *IEEE Transactions on Computational Imaging*, vol. 7, pp. 849–863, 2021.
- [12] U. S. Kamilov, C. A. Bouman, G. T. Buzzard, and B. Wohlberg, "Plug-and-Play Methods for Integrating Physical and Learned Models in Computational Imaging," *arXiv preprint arXiv:2203.17061*, 2022.
- [13] K. Gregor and Y. LeCun, "Learning fast approximations of sparse coding," in *Proceedings of the 27th international conference on international conference on machine learning*, 2010, pp. 399–406.
- [14] H. K. Aggarwal, M. P. Mani, and M. Jacob, "MoDL: Model-based deep learning architecture for inverse problems," *IEEE transactions on medical imaging*, vol. 38, no. 2, pp. 394–405, 2018.
- [15] J. Xiang, Y. Dong, and Y. Yang, "FISTA-net: Learning a fast iterative shrinkage thresholding network for inverse problems in imaging," *IEEE Transactions on Medical Imaging*, vol. 40, no. 5, pp. 1329–1339, 2021.
- [16] Y. Yang, J. Sun, H. Li, and Z. Xu, "Deep ADMM-Net for compressive sensing MRI," *Advances in neural information processing systems*, vol. 29, 2016.
- [17] S. Bai, J. Z. Kolter, and V. Koltun, "Deep equilibrium models," *Advances in Neural Information Processing Systems*, vol. 32, 2019.
- [18] D. Gilton, G. Ongie, and R. Willett, "Deep equilibrium architectures for inverse problems in imaging," *IEEE Transactions on Computational Imaging*, vol. 7, pp. 1123–1133, 2021.
- [19] V. Antun, F. Renna, C. Poon, B. Adcock, and A. C. Hansen, "On instabilities of deep learning in image reconstruction and the potential costs of AI," *Proceedings of the National Academy of Sciences*, vol. 117, no. 48, pp. 30088–30095, 2020.
- [20] J. Yang, Y. Zhang, and W. Yin, "A fast alternating direction method for TVL1-L2 signal reconstruction from partial Fourier data," *IEEE Journal of Selected Topics in Signal Processing*, vol. 4, no. 2, pp. 288–297, 2010.
- [21] I. Daubechies, M. Debrise, and C. De Mol, "An iterative thresholding algorithm for linear inverse problems with a sparsity constraint," *Communications on Pure and Applied Mathematics: A Journal Issued by the Courant Institute of Mathematical Sciences*, vol. 57, no. 11, pp. 1413–1457, 2004.
- [22] A. Beck and M. Teboulle, "A fast iterative shrinkage-thresholding algorithm for linear inverse problems," *SIAM journal on imaging sciences*, vol. 2, no. 1, pp. 183–202, 2009.
- [23] J. Zhang and B. Ghanem, "ISTA-Net: Interpretable optimization-inspired deep network for image compressive sensing," in *Proceedings of the IEEE conference on computer vision and pattern recognition*, 2018, pp. 1828–1837.
- [24] K. Hammernik *et al.*, "Learning a variational network for reconstruction of accelerated MRI data," *Magnetic resonance in medicine*, vol. 79, no. 6, pp. 3055–3071, 2018.
- [25] H. Heaton, S. Wu Fung, A. Gibali, and W. Yin, "Feasibility-based fixed point networks," *Fixed Point Theory and Algorithms for Sciences and Engineering*, vol. 2021, no. 1, pp. 1–19, 2021.
- [26] E. K. Ryu and S. Boyd, "Primer on monotone operator methods," *Appl. Comput. Math.*, vol. 15, no. 1, pp. 3–43, 2016.
- [27] E. Winston and J. Z. Kolter, "Monotone operator equilibrium networks," *Advances in neural information processing systems*, vol. 33, pp. 10718–10728, 2020.
- [28] L. Bungert, R. Raab, T. Roith, L. Schwinn, and D. Tenbrinck, "CLIP: Cheap Lipschitz training of neural networks," in *International Conference on Scale Space and Variational Methods in Computer Vision*. Springer, 2021, pp. 307–319.
- [29] R. Souza *et al.*, "An open, multi-vendor, multi-field-strength brain MR dataset and analysis of publicly available skull stripping methods agreement," *NeuroImage*, vol. 170, pp. 482–494, 2018.
- [30] C. Chen *et al.*, "OCMR (v1. 0)–Open-Access Multi-Coil k-Space Dataset for Cardiovascular Magnetic Resonance Imaging," *arXiv preprint arXiv:2008.03410*, 2020.
- [31] Z. Wang, A. C. Bovik, H. R. Sheikh, and E. P. Simoncelli, "Image quality assessment: from error visibility to structural similarity," *IEEE transactions on image processing*, vol. 13, no. 4, pp. 600–612, 2004.
- [32] K. P. Pruessmann, M. Weiger, M. B. Scheidegger, and P. Boesiger, "SENSE: sensitivity encoding for fast MRI," *Magnetic Resonance in Medicine: An Official Journal of the International Society for Magnetic Resonance in Medicine*, vol. 42, no. 5, pp. 952–962, 1999.
- [33] O. Ronneberger, P. Fischer, and T. Brox, "U-net: Convolutional networks for biomedical image segmentation," in *International Conference on Medical image computing and computer-assisted intervention*. Springer, 2015, pp. 234–241.